J Mater Sci (2009) 44:3305–3314
DOI 10.1007/s10853-009-3446-3

# Isothermal fatigue behavior of cast superalloy Inconel 792-5A at 23 and 900 °C

**Karel Obrtlík · Martin Petrenec · Jiří Man ·**
**Jaroslav Polák · Karel Hrbáček**

Received: 10 July 2008 / Accepted: 27 March 2009 / Published online: 15 April 2009

**Abstract** Total strain-controlled tests have been performed on cylindrical specimens of polycrystalline Inconel 792-5A at 23 and 900 °C to study the effect of temperature on low cycle fatigue characteristics and cyclic strain localization. Hardening/softening curves, cyclic stress–strain curves, and fatigue life curves are presented. Two linear dependencies are used to approximate the room temperature data in Manson–Coffin plot. Technique of oriented foils observed in transmission electron microscope is used to study dislocation structure. Effect of temperature on surface relief topography and fracture surface is documented using scanning electron microscopy and atomic force microscopy. High-amplitude straining is characterized by slight initial hardening followed by saturation at room temperature and sustained weak softening at 900 °C. Low-amplitude cycling results in the stable stress response. Plastic strain localization into persistent slip bands lying along {111} slip planes was observed at both temperatures.

## Introduction

Inconel 792-5A nickel-base superalloy is a cast high-strength polycrystalline material designed for the production of blades and discs of gas turbine engines for use at temperatures up to about 950 °C. It offers excellent corrosion resistance in sulfur-bearing environments [1, 2]. The critical turbine parts are subjected to repeated elastic–plastic straining as a result of heating and cooling during start-up and shutdown periods. Consequently, low-cycle fatigue is an important consideration in the design of the components, and cyclic stress–strain and fatigue life data at temperatures up to high temperatures are needed. Fatigue behavior of Inconel 792-5A is reported scarcely [3, 4].

Onset of strain localization is a decisive step in the fatigue damage evolution of crystalline materials. Strain localization manifests itself in specific changes of internal structure and in the formation of the characteristic surface relief [5]. Nickel-base superalloys are composite materials consisting of softer $\gamma$ solid solution matrix and harder strengthening coherent precipitates; therefore, cyclic strain is localized predominantly in the softer phase. Besides, slip markings and slip bands, running parallel to the active slip plane, have been reported in many nickel-base superalloy single crystals (for review see [6]) and polycrystals [7–18].

Dislocation structure investigations in superalloy polycrystals cycled at room and high temperatures [7–17] indicate planar slip bands going parallel to {111} slip planes and cutting the strengthening particles. Narrow slip bands were observed even at 950 °C [12]. Surface slip markings that originate in the vicinity of the slip band intersection with the free surface were found on superalloy specimens both after room-temperature [7, 8, 11, 13, 18] and high-temperature cycling [15, 17].

Recently, atomic force microscopy (AFM) was applied to study surface topography of fatigued metallic materials [17–27]. This new, sensitive technique can provide quantitative information on the three-dimensional surface relief with resolution approaching atomic scale. It can help to elucidate the crucial questions in cyclic strain localization of nickel-base superalloys, namely whether and to what

K. Obrtlík (✉) · M. Petrenec · J. Man · J. Polák
Institute of Physics of Materials, AS CR, Žižkova 22,
616 62 Brno, Czech Republic
e-mail: obrtlik@ipm.cz

K. Hrbáček
První brněnská strojírna Velká Bíteš, a.s., Vlkovská 279,
595 12 Velká Bíteš, Czech Republic

extent the slip bands observed are persistent. AFM was used to investigate the surface relief of superalloy polycrystals at room temperature [17, 18] and also at high temperature [17].

This article reports fatigue behavior of Inconel 792-5A polycrystals under symmetrical total strain cycle at room temperature and at 900 °C. This article focuses on the effect of high temperature on the cyclic stress–strain response and fatigue life curves. Special attention is devoted to the investigation of cyclic strain localization at both temperatures using scanning electron microscopy (SEM), AFM, and transmission electron microscopy (TEM) with the aim to reveal differences in surface relief morphology at both temperatures and to elucidate whether relevant slip bands are persistent.

## Experimental

### Material, specimens, and testing

Inconel 792-5A polycrystals were provided by PBS Velká Bíteš, a.s. as conventionally cast rods in fully heat-treated condition, i.e., after 1120 °C/4 h/rapid air cooling (RAC) + 1080 °C/4 h/AC + 845 °C/24 h/AC. Chemical composition of the superalloy is shown in Table 1. Polished sections of the material reveal coarse grains with dendrites, carbides, and shrinkage pores being rarely up to 0.5 mm in diameter [28]. Structure of the alloy is shown in Fig. 1. Rugged grain boundaries due to the complex dendritic structure are apparent in the optical micrograph of the section parallel to the rod axis in Fig. 1a. The average grain size, found using the linear intercept method, was 3.0 mm. The heat treatment yielded duplex $\gamma'$ microstructure consisting of cuboidal and spherical $\gamma'$ precipitates embedded in a solid solution-strengthened $\gamma$ matrix—see Fig. 1b. The average size of $\gamma'$ particles is 0.2 µm (diameter for spherical particles) and 0.6 µm (cube edge for cuboidal precipitates). The fcc $\gamma$ phase is coherent with the $\gamma'$ phase having an ordered L1$_2$ structure [1].

Figure 2 shows button-end specimens having gauge length and diameter of 15 and 6 mm, respectively, used in fatigue tests. Specimens were machined parallel to the rod axis and their gauge length was mechanically ground. The gauge section of some specimens was electrolytically polished to facilitate the surface relief observation.

The specimens were fatigued in a computer-controlled electrohydraulic testing system in a symmetrical push–pull cycle under strain control ($R_\varepsilon = -1$). Continuous cycling with the triangular time dependence of the total strain was applied. The strain was measured and controlled using a sensitive extensometer with a 12 mm base. The strain rate of $2 \times 10^{-3}$ s$^{-1}$ and total strain amplitude were kept constant in all tests. The room-temperature (23 °C) and high-temperature (900 °C) isothermal tests were conducted in air. Heating was provided by a three-zone resistance furnace and monitored by three thermocouples attached to both specimen ends and to the upper part of the gauge section. The hysteresis loops for selected numbers of cycles were saved to disk memory. Plastic strain amplitude derived from the half of the loop width and stress amplitude at half-life was evaluated.

### TEM, SEM, and AFM observations

TEM of thin foils was adopted to study internal dislocation structure in the superalloy. A Philips CM-12 operating at 120 kV with a double tilt holder was used. Thin foils were prepared using the standard double jet technique from slices cut in the specimen gauge area parallel to the specimen

**Table 1** Chemical composition of Inconel 792-5A (in wt%)

| Cr | Co | Ti | Al | Ta | W | Mo | Fe | Nb | C | Zr | B | Ni |
|---|---|---|---|---|---|---|---|---|---|---|---|---|
| 12.28 | 8.87 | 3.98 | 3.36 | 4.12 | 4.10 | 1.81 | 0.16 | 0.10 | 0.078 | 0.031 | 0.015 | Bal. |

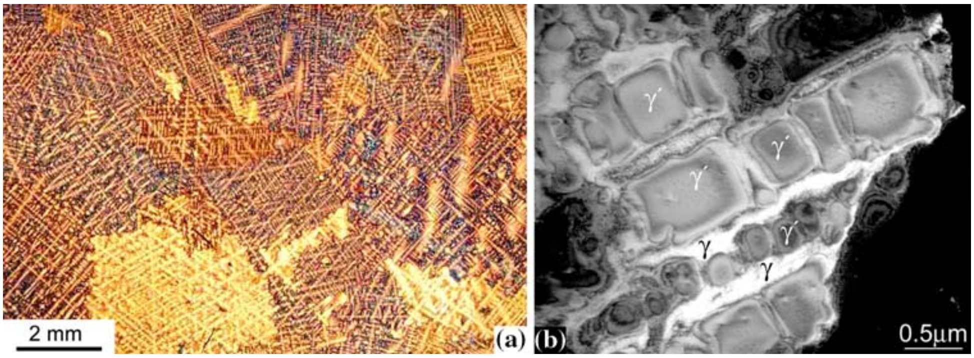

**Fig. 1** Microstructure of the material. **a** Section parallel to the loading axis (optical microscope). **b** Detailed structure of precipitates (TEM)

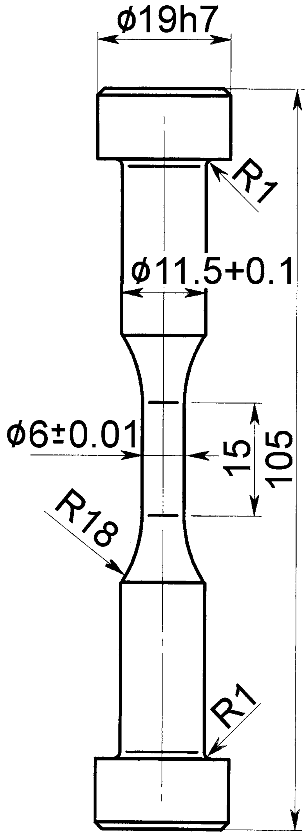

**Fig. 2** Shape and dimensions of the specimen (in mm)

axis. Slices with a thickness of 0.8 mm were ground mechanically to a thickness of about 80 μm. Discs with a diameter of 3 mm were cut from the slices and then thinned using double jet technique until perforation appeared. Special care was taken to mark the direction of the specimen axis, so that the orientation of each grain relative to the loading axis could be determined using diffraction patterns and Kikuchi lines. We have adopted the usual notation in which the loading axis is within the basic stereographic triangle (001), $(\bar{1}11)$, and (011).

Surface relief observations were performed in Philips 505 and JEOL 6460 SEMs and in the Accurex IIL AFM on the gauge length of selected specimens. AFM in contact imaging mode in the air was used to obtain constant-force topographic images. A standard silicon nitride cantilever with a pyramidal tip, from Park Scientific Instruments, having the radius of curvature of 20 nm and the vertex angle of 36° was applied. The crystallographic orientation of selected grains was determined in the SEM using the electron backscattering diffraction (EBSD). The method based on the analysis of the Kikuchi patterns of backscattered electrons is described elsewhere [22, 29]. Fracture surfaces were studied using JEOL 6460 SEMs.

## Results

### Stress–strain response and fatigue life

Figure 3 shows the stress amplitude $\sigma_a$ as a function of the number of cycles $N$ obtained at room temperature and at 900 °C for different total strain amplitudes. The character of these hardening/softening curves varies with strain amplitude and temperature. For room-temperature cycling, the initial hardening is followed by the stable stress response—see Fig. 3a. The hardening becomes more pronounced with increasing strain amplitudes. High-amplitude cycling at high temperature results in slow softening up to the end of the fatigue life while the saturated behavior can be seen in the low-amplitude domain—see Fig. 3b.

Cyclic stress–strain curve (CSSC) of the material is shown in Fig. 4 for both temperatures. The stress amplitude is plotted vs. the plastic strain amplitude at half-life. Experimental data were approximated by the power law

$$\log \sigma_a = \log K' + n' \log \varepsilon_{ap}\cdot \qquad (1)$$

Fatigue-hardening coefficient $K'$ and fatigue-hardening exponent $n'$ were evaluated using linear regression analysis and are shown together with standard errors in Table 2. It can be seen that the CSSC strongly depends on temperature. For a given plastic strain amplitude, the stress amplitude at room temperature is about twice as that at

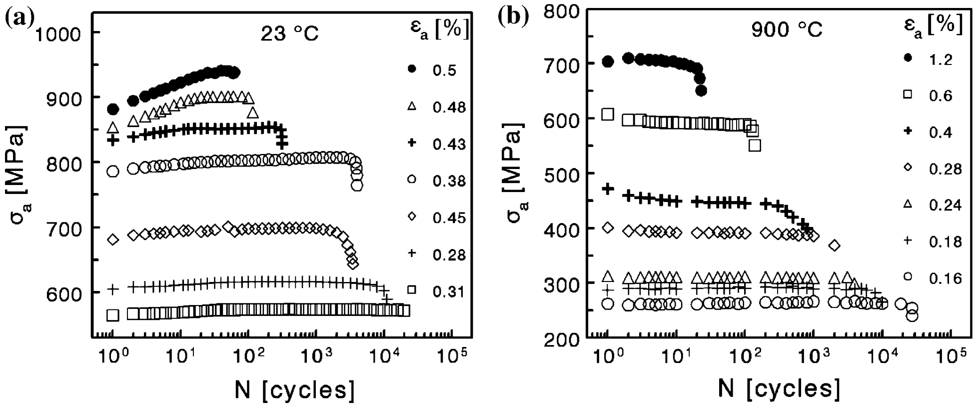

**Fig. 3** Cyclic hardening/softening curves of Inconel 792-5A. **a** 23 °C. **b** 900 °C

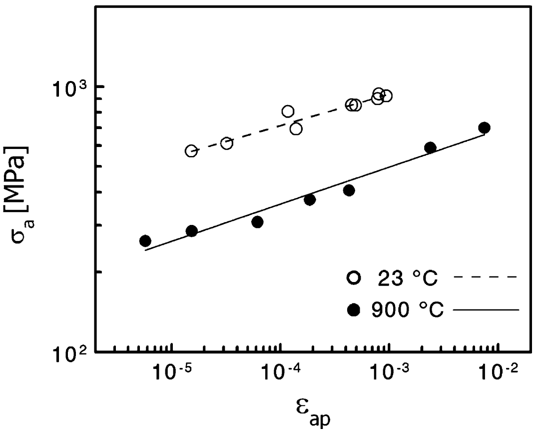

**Fig. 4** Cyclic stress–strain curve of Inconel 792-5A at two temperatures

**Table 2** Parameters of cyclic stress–strain, Manson–Coffin, and Basquin curves of Inconel 792-5A

| Temperature (°C) | 23 | 900 |
|---|---|---|
| $K'$ (MPa) | 2130 + 220<br>− 200 | 1310 + 150<br>− 130 |
| $n'$ | 0.118 ± 0.012 | 0.140 ± 0.012 |
| $\varepsilon'_f$ | | 7.0 + 14.8<br>− 4.8 |
| $c$ | | −1.27 ± 0.13 |
| $\varepsilon'_{fI}$ | 0.0109 + 0.0034<br>− 0.0026 | |
| $c_I$ | −0.500 ± 0.041 | |
| $\varepsilon'_{fII}$ | 6.8 + 1.1<br>− 1.0 | |
| $c_{II}$ | −1.21 ± 0.02 | |
| $\sigma'_f$ (MPa) | 1480 + 140<br>− 130 | 1580 + 260<br>− 230 |
| $b$ | −0.086 ± 0.012 | −0.169 ± 0.017 |

900 °C. The value of the fatigue-hardening exponent $n'$ is almost the same for both temperatures.

Fatigue life curves are plotted in Fig. 5 for both temperatures. Figure 5a shows the plastic strain amplitude $\varepsilon_{ap}$ at half-life vs. the number of cycles to fracture $N_f$ in the bilogarithmic representation. Manson–Coffin law

$$\varepsilon_{ap} = \varepsilon'_f (2N_f)^c \tag{2}$$

is commonly used to describe the low-cycle fatigue life. $\varepsilon'_f$ is the fatigue ductility coefficient and $c$ is the fatigue ductility exponent. Because the fatigue life $N_f$ is the dependent variable and $\varepsilon_{ap}$ is the independent variable, Eq. 2 is written in the form suitable to fit experimental data

$$Y = (X - \log \varepsilon'_f)/c \tag{3}$$

where $Y = \log(2N_f)$ and $X = \log \varepsilon_{ap}$. Nonlinear regression analysis is applied to evaluate parameters $\varepsilon'_f$ and $c$ that are shown together with their standard errors in Table 2. Room temperature experimental data can be divided into high-amplitude domain I and low-amplitude domain II. Manson–Coffin law (3) is fitted to fatigue life data for each domain separately. It can be seen that the fatigue lives measured at both temperatures in the Manson–Coffin representation differ significantly only at high amplitudes. The values of the Manson–Coffin law parameters obtained at 900 °C and in the domain II at room temperature are almost identical—see Table 2.

Fatigue life curves in the representation of the stress amplitude $\sigma_a$ at half-life vs. the number of cycles to fracture $N_f$ are shown in Fig. 5b. The Basquin law is expressed by analogy to the Manson–Coffin law (see Eq. 3) in the form

$$Y = (Z - \log \sigma'_f)/b \tag{4}$$

where $Y = \log(2N_f)$ and $Z = \log \sigma_a$. Equation 4 is used to fit experimental data and evaluate the fatigue strength coefficient, $\sigma'_f$, and the fatigue strength exponent, $b$. Their values are shown in Table 2. The Basquin curves strongly depend on temperature—see Fig. 5b and Table 2. The absolute value of the fatigue strength exponent at 900 °C is almost twice as that obtained at room temperature while the fatigue strength coefficient value is equal at both temperatures within experimental scatter. The increase in temperature from room temperature to 900 °C results in considerable reduction of the stress amplitude, e.g., for $N_f = 5000$ cycles, the stress amplitude at 900 °C is half of that at room temperature.

## Surface relief, dislocation structure, and fractography

Surface relief of specimens cycled to failure at both temperatures has been studied in SEM and AFM. Figure 6 shows SEM micrographs of the surface of a specimen cycled with high strain amplitude ($\varepsilon_a = 0.6\%$, $\varepsilon_{ap} = 0.08\%$ at half-life) at room temperature. Thin parallel slip markings going through both the $\gamma$ matrix and the $\gamma'$ precipitates can be seen on the etched surface of a large grain in Fig. 6a. They are spaced nearly equidistantly and are separated by almost nondeformed surface. With decreasing strain amplitude the number of slip markings is reduced. Slip markings were not observed in all grains even in specimens cycled with very high strain amplitudes that correspond to the fatigue life close to 100 cycles. They lie exclusively parallel to the {111} slip plane traces. The surface relief in majority of grains corresponds to the activation of one slip system. Fatigue cracks initiated either in the grain interior along slip markings or in grain

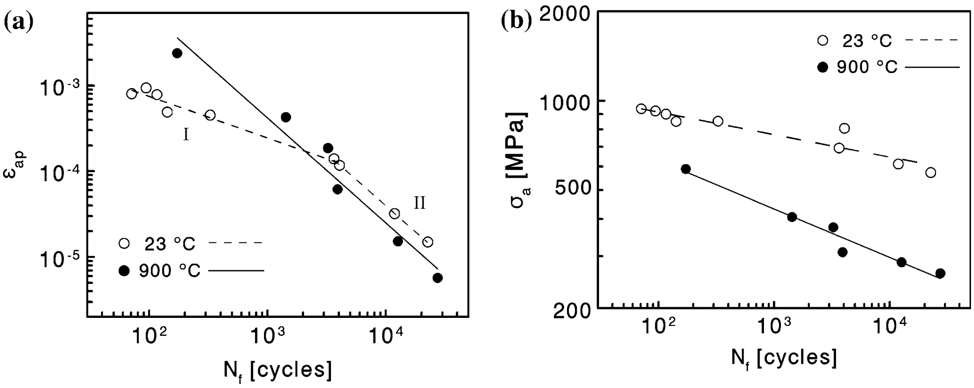

**Fig. 5** Fatigue life curves in (**a**) Manson–Coffin and (**b**) Basquin representation of Inconel 792-5A at two temperatures

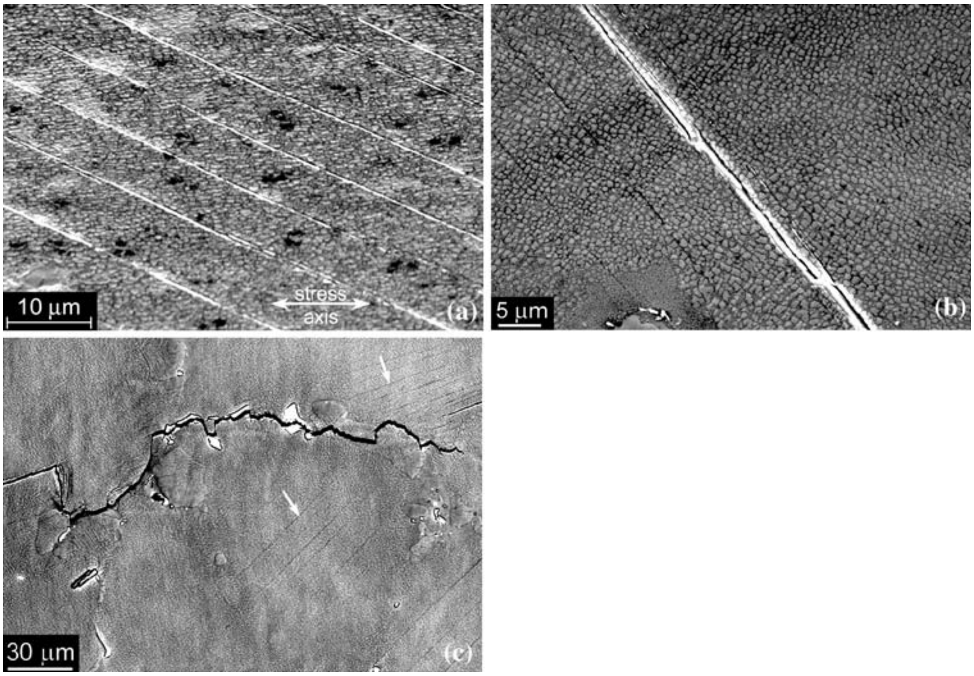

**Fig. 6** SEM micrographs of surface relief of a specimen cycled to fracture at room temperature with $\varepsilon_a = 0.6\%$. **a** Slip markings. **b** Crack initiation at slip markings. **c** Crack initiation at grain boundaries

boundaries. Figure 6b shows a fatigue crack initiated along the slip markings. The crack is formed by linking three segments each of which run along a different parallel slip marking in the grain. A fatigue crack initiated at a dendritic grain boundary is shown in Fig. 6c. One slip system, with slip markings indicated by white arrows, is activated in each of both grains whose fractions can be seen in Fig. 6c.

Figure 7 shows the most pronounced surface relief obtained at 900 °C which developed in a grain oriented for single slip (the stress axis of the grain is $[\bar{3}, 7, 10]$) in a specimen cycled with high strain amplitude ($\varepsilon_a = 1.2\%$, $\varepsilon_{ap} = 0.75$ % at half-life). It can be seen from Fig. 7a that the slip markings are short, wide, wavy, and densely populated in comparison with those obtained at room temperature. They do not lie along a particular crystal plane trace and they are inclined at an angle up to 10° to each other. Number of grains with slip markings is very low in comparison with that found at room temperature. Well-developed slip markings were observed only in a few grains of the specimen cycled with the highest strain amplitude at 900 °C. Figure 7b shows intrusions or initiated cracks in the central part of slip markings with extrusions on both sides. However, fatigue cracks initiated predominantly at the boundary of dendritic grains. Later formation of the main crack includes the mechanism of crack linking; both the grain boundary cracks and those within the slip markings participate in the formation of the principal crack.

AFM micrographs show a more detailed view of surface topography. Surface relief in 3D representation typical for both temperatures is shown in Fig. 8. Quantitative data on the surface relief can be evaluated using surface profiles shown in Fig. 9. Different scales in horizontal and vertical direction are used in Figs. 8 and 9. The surface profiles correspond to the sections perpendicular to both the surface slip markings and to the surface. The black arrows in Fig. 8

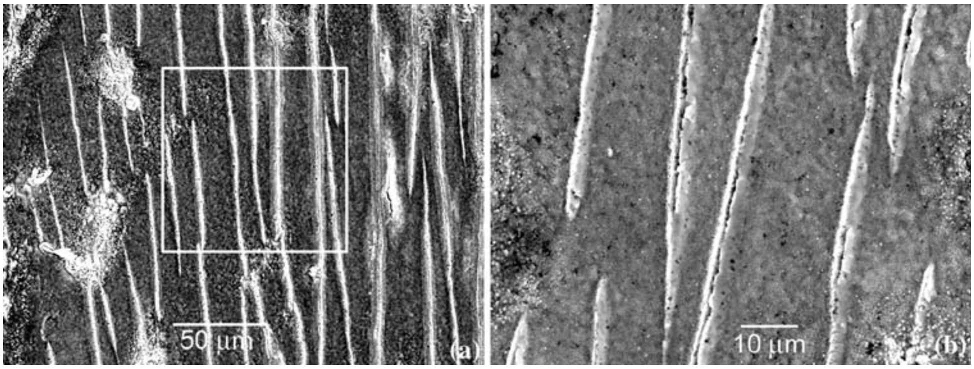

**Fig. 7** Surface relief in a specimen fatigued with $\varepsilon_a = 1.2\%$ at 900 °C (SEM). **a** Slip markings. **b** Crack initiation within slip markings

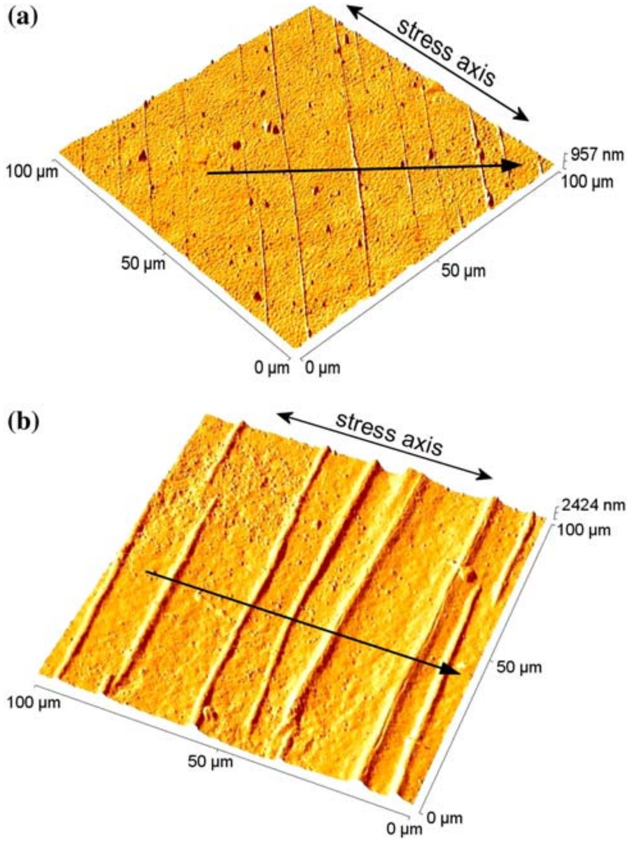

**Fig. 8** Three-dimensional AFM micrograph of surface relief of specimen fatigued to the end of life. **a** $\varepsilon_a = 0.6\%$, 23 °C. **b** Surface area marked by *white box* in Fig. 7a, $\varepsilon_a = 1.2\%$, 900 °C

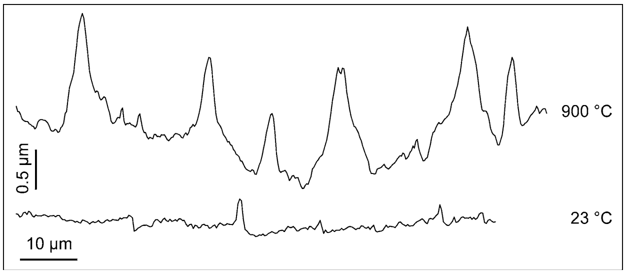

**Fig. 9** Surface relief profiles in sections perpendicular to the slip markings (indicated by *black arrows* in Fig. 8)

denote positions of the sections. AFM observation revealed clear extrusions along slip marking at both temperatures—see Figs. 8 and 9. The presence of extrusions suggests that the corresponding slip bands are persistent—comp. discussion in the following section. The morphology of individual slip markings observed at room temperature differs considerably—see Figs. 8a and 9. Surface profile (see Fig. 9) shows negligible relief at the first slip marking from the left while a clear step is apparent at the second slip marking, and well-developed extrusion with the maximum height of 0.4 µm is identified at the third slip marking. The height of extrusions varies markedly along slip markings as well. Different morphology of surface relief is observed at 900 °C—see Figs. 8b and 9. Figure 8b shows in detail the surface relief within the box area of Fig. 7a. Compact cord-like extrusions can be seen along all slip markings in Fig. 8b. They are higher and wider in comparison with those obtained at room temperature. Small undulation of specimen surface is apparent between individual slip markings. The height of majority of extrusions exceeds 1 µm and changes only slowly along the slip marking. The maximum extrusion height was estimated to 1.6 µm.

Internal dislocation structure was studied by TEM with the aim to reveal inhomogeneous dislocation microstructure related to cyclic strain localization observed on the free surface. Examples of dislocation arrangements are shown in Fig. 10. Figure 10a shows dislocation structure in a specimen cycled at room temperature to the end of life ($\varepsilon_a = 0.5\%$, $\varepsilon_{ap} = 0.08\%$ at half-life). Inhomogeneous dislocation arrangement is apparent in Fig. 10a in a grain oriented for single slip (stress axis is indicated within the embedded standard stereographic triangle). Numerous thin bands (thickness below 0.1 µm) of high dislocation density are separated by low dislocation density areas. The bands run parallel to the primary slip plane cutting both the $\gamma$ channels and the $\gamma'$ particles. Bundles of high dislocation density are often formed between closely spaced neighboring bands. In the low dislocation density areas,

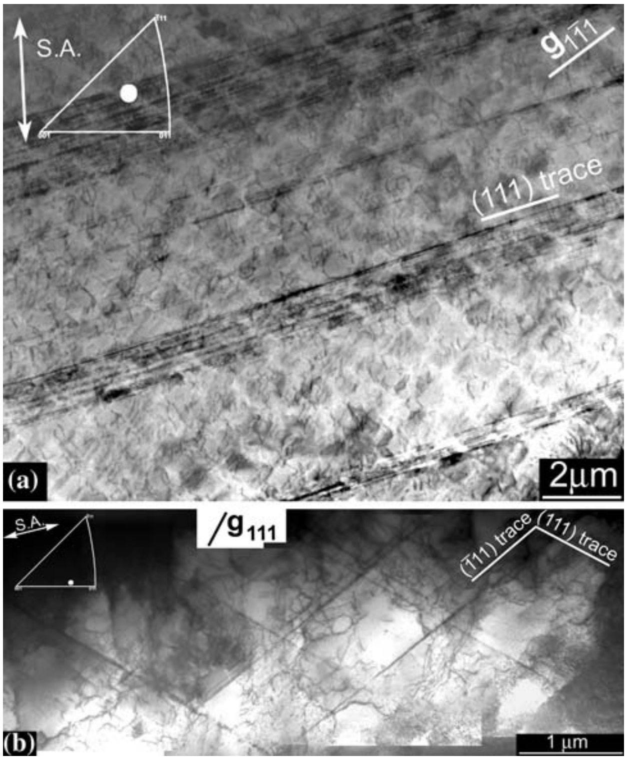

**Fig. 10** TEM micrographs of dislocation arrangement in specimens cycled to fracture. *S.A.* stress axis. **a** $\varepsilon_a = 0.5\%$, 23 °C, foil plane is close to $(\bar{1}01)$. **b** $\varepsilon_a = 1.2\%$, 900 °C, foil plane is $(3\bar{3}2)$

dislocations are present within the $\gamma'$ precipitates but predominantly in the $\gamma$ channels. Figure 10b shows dislocation arrangement in specimen cycled at 900 °C with strain amplitude $\varepsilon_a = 1.2\%$ ($\varepsilon_{ap} = 0.75\%$ at half-life). Thin slip bands running parallel to the primary slip plane (111) and to the secondary most stressed $(\bar{1}11)$ plane can be seen in a grain oriented for double slip. By analogy to room-temperature cycling, the bands pass through both the matrix and the precipitates.

Fracture surface observation with SEM reveals that fatigue cracks initiate from the surface frequently at casting defects present close to the surface at both temperatures. Cracks initiate at several sites of a specimen, but usually one crack results in final fracture. Smooth facets inclined to the loading axis observed in fracture surfaces close to specimen surface can be identified with the stage I crack growth. The stage II crack growth is characterized by a mixture of intergranular and transgranular fracture with a preponderance of the latter. An example of fracture surfaces corresponding to the stage II crack growth is shown in Fig. 11. At room temperature, a typical fracture consists of many facets along crystal planes predominantly of one type (Fig. 11a). At 900 °C, the ductile fracture with fields of striations is a typical feature. The amount of striations increases with increasing crack length (Fig. 11b).

## Discussion

### Cyclic strain localization, crack initiation, and growth

Experimental study of surface topography using SEM and AFM and investigation of internal dislocation structure in TEM of Inconel 792-5A fatigued under total strain control revealed pronounced strain localization both at room temperature and at 900 °C. On the surface, strain localization manifests in surface slip markings the characteristics of which depend on temperature. In the bulk, planar slip bands of high dislocation density are observed at both temperatures. They run parallel to the primary slip plane (111) and pass through both the $\gamma$ channels and the $\gamma'$-ordered particles. These findings of strain localization are generally consistent with previous works on different superalloys [6–18].

The SEM and AFM observation of surface relief in Inconel 795-5A at both temperatures (see Figs. 6, 7, 8, 9) revealed distinct hilly extrusions within slip markings that arise where slip bands emerge on the free surface. The extrusions are reminiscent of those in persistent slip markings (PSMs) of single-phase FCC metals [5]. Extrusion growth rate was assessed quantitatively at room temperature in polycrystalline copper [30] and in austenitic

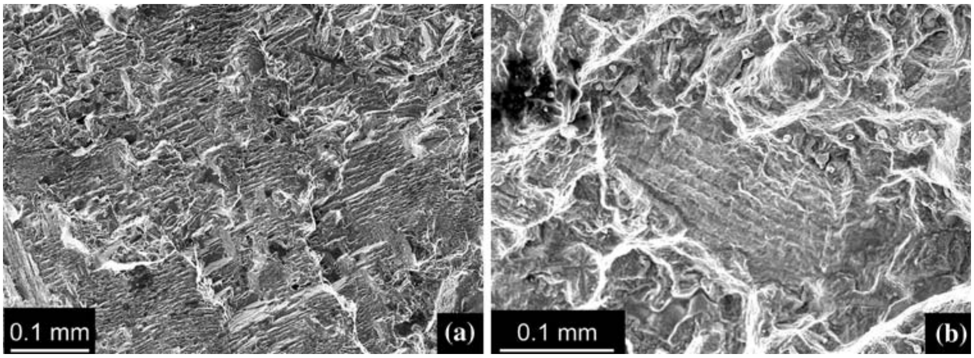

**Fig. 11** SEM fractographs of Inconel 792-5A. **a** $\varepsilon_a = 0.48\%$, 23 °C. **b** $\varepsilon_a = 0.6\%$, 900 °C

stainless steel 316L [24]. Its highest values were estimated at the beginning of cycling as 0.4 nm/cycle in Cu and 0.081 nm/cycle in 316L steel. These values agree well with the evolution of the average extrusion height assessed in Waspaloy at room temperature [18]. Maximum extrusion height evaluated in this work using AFM measurements is 400 nm at room temperature and 1600 nm at 900 °C. Therefore, the morphology and the height of extrusions witness indirectly that the relevant slip bands are persistent, i.e., they are active for many cycles in the course of the fatigue life.

Evaluation of AFM measurements of surface relief in this work shows that the maximum extrusion height at 900 °C is four times higher than that obtained at room temperature (compare Fig. 9). This finding supports the vacancy models of surface relief formation based on mass redistribution [31, 32]. Vacancies that form in a persistent slip band (PSB) by interaction of moving dislocations migrate out of the slip band and atoms diffuse in the opposite direction to the band. Both the vacancy migration out of the band and the reverse flow of atoms to the band contribute to the extrusion growth [31, 32]. The diffusion flow strongly increases with increasing temperature, which results in the more pronounced surface relief at higher temperature in agreement with experimental observation at 900 °C in this work. The present results also agree with the recent AFM observation of surface relief in Inconel 713 LC cyclically strained to the end of the fatigue life at four temperatures [17]. The highest extrusions were found at the highest temperature of 800 °C.

The PSMs are observed to be wavy after fatigue test at the temperature of 900 °C while almost straight PSMs are apparent at room-temperature cycling—see Figs. 6 and 7. Thus, the temperature increase from room temperature to 900 °C results in the change from planar slip to wavy slip behavior of Inconel 792-5A. However, only straight and narrow slip bands parallel to {111} slip planes and cutting precipitates have been found in the interior of the material at both temperatures—see Fig. 10. The wavy slip and planar slip behavior in single-phase metals is usually associated with easy and difficult cross slip, respectively [33]. In Ni-base superalloys, the wavy slip markings are observed in tensile test specimens even at room temperature [34]. Their occurrence is associated with changes in the width of $\gamma$ channels, and depends on the crystal and dendrites orientation. The macroscopic deviation of slip markings from {111} planes observed at 900 °C can be explained by multiple cross slip on octahedral slip planes within $\gamma$ channels and/or by cross slip onto cubic planes in agreement with earlier suggestions for different Ni-base superalloys [35–37].

Intensive cyclic plastic strain in PSBs results in crack initiation within PSMs. The stress concentration between two neighboring intrusions can lead to the formation of new surfaces, and a half-elliptical crack is nucleated [38]. The half-elliptical cracks can link and grow under local slip–unslip mechanism along the primary slip plane (mode II) with the assistance of a corrosive environment that prevents the rewelding of new surfaces. This stage I crack growth corresponds to smooth facets inclined to the loading axis observed in fracture surfaces close to the specimen surface of Inconel 792-5A. Grain boundary crack initiation is observed in the material as well. It is the decisive mechanism at 900 °C. The intersection of a grain boundary with a free surface is a site of preferential diffusion of oxidizing gases, resulting in the notch development and subsequent crack nucleation under the action of cyclic stress. Crack initiation both at grain boundaries and PSMs is accelerated by casting defects present at the specimen surface or close to it.

Later, the transition to the stage II crack growth takes place, and a crack propagates approximately perpendicularly to the stress axis. Crack growth proceeds mostly transgranularly, and the crack linking with initiated cracks and interaction with localized strain regions are important mechanisms. Present SEM observations suggest that operating slip planes play significant role in the fatigue fracture at room temperature (Fig. 11a), and the crack tip blunting occurs at 900 °C (Fig. 11b). Fatigue–environment interaction must be taken into account to advance crack propagation particularly at high temperature [39, 40].

## Stress–strain response and fatigue life

Influence of material structure, particularly of structural changes evolved due to cyclic straining, on phenomenological fatigue characteristics is discussed in this section. Stress–strain response, two slopes in the Manson–Coffin plot, a high absolute value of the fatigue ductility exponent, and scatter in experimental data are addressed topics.

Present results show initial hardening followed by stable stress response in room temperature cycling and slight permanent softening at 900 °C—see Fig. 3. Microstructural changes found in the natural composite of Inconel 792-5A in the form of PSBs in the interior and PSMs at the surface at both temperatures manifest themselves in the cyclic behavior of the superalloy. The PSBs accommodate cyclic plastic strain more effectively in comparison with initial dislocation arrangement formed of dislocations moving predominantly in the $\gamma$ channels that are approximately parallel to {001} planes. Consequently, the formation of PSBs in the high-amplitude domain leads to the stabilization of the stress response at room temperature and even to the cyclic softening observed at 900 °C where the degree of localization is higher.

The present results show that the fatigue life in the Manson–Coffin representation is almost temperature independent in the low-amplitude domain— see Fig. 5a. In the high-amplitude domain for the same fatigue life, a drop in plastic strain amplitude is clearly apparent at room temperature in comparison with values obtained at 900 °C. The difference in the fatigue life data for room temperature and 900 °C can be a direct consequence of the hardening/softening behavior of Inconel 792-5A, shown in Fig. 3. Namely, pronounced hardening at room temperature and slow softening at 900 °C are evident in the high-amplitude domain while saturated stress response is typical for the low amplitudes at both temperatures. Since plastic strain amplitude at half-life is applied to construct the Manson–Coffin plot, the hardening/softening behavior can explain qualitatively the difference between fatigue life curves at room temperature and 900 °C in the high–amplitude domain. The experimental data at room temperature suggest two slopes in the Manson–Coffin curve in agreement with previous results on various Ni-base superalloys. The two-slope behavior is attributed to a change in deformation mechanism with strain amplitude variation [8, 13, 15].

Figure 5 and Table 2 show another interesting feature of the fatigue life curves, namely, the comparatively high absolute value of the fatigue ductility exponent $c$ in the Manson–Coffin law at 900 °C and at room temperature in the low-amplitude domain. The fatigue ductility exponent close to $c \sim -1$ is referred in some Ni-base superalloys [5, 13, 15, 41], but its value over many metallic materials lies around $-0.6$ [5, 42]. The value $c = -1$ implies the cumulative plastic strain to fracture is independent of the plastic strain amplitude. Plastic strain amplitude at a given number of cycles to fracture in Inconel 792-5A with its over 50 vol.% of hard precipitates is almost two orders of magnitude lower in comparison with simple ductile metals, e.g., 316L stainless steel [43]. It is accommodated prevailingly in the softer $\gamma$ solid solution with the exception of the high strain domain at room temperature. Density of slip markings at 900 °C and in the low-amplitude domain at room temperature is very low. Recently, Obrtlík et al. [44] have reported detailed study of surface relief topography in $\langle 001 \rangle$-oriented single crystal CMSX-4 and have shown that only about every 20th horizontal $\gamma$ channel forms a clear slip marking. This finding, though not documented in polycrystals, helps to clarify the low plastic strain in some superalloys. Mughrabi [45] has shown that the average plastic strain in PSBs in the plateau regime of single crystals does not depend on the applied plastic strain amplitude. Application of this finding to the localized regions in the Inconel 792-5A $\gamma$ solid solution supports high absolute value of the fatigue ductility exponent. Namely, pronounced strain localization in the superalloy leads to the low probability of interaction between individual localized regions which results in the independence of cumulative plastic strain to fracture from the applied plastic strain amplitude and in the fatigue ductility exponent close to $-1$. Moreover, the presence of casting defects in the material makes the strain localization more intensive and thus contributes to the high absolute value of the fatigue ductility exponent in the low-amplitude domain.

There is a large scatter of experimental points in the fatigue life curves. An important component of the scatter can be related to the influence of casting defects in the material. The casting defects substantially reduce crack initiation period due to stress concentration. The scatter turns out to be particularly pronounced in the high cycle fatigue of cast large grain superalloys [46, 47]. Moreover, the low number of grains present in the gauge length can result in different stress–strain response of individual specimens. The axial applied stress $\sigma$ can be related to the average resolved shear stress $\bar{\tau}$ by the relation $\sigma = \bar{\tau}/\mu_e$ where $\mu_e$ is an effective Schmid factor that depends on the plastic strain [5, 48]. By analogy, the axial plastic strain $\varepsilon_p$ is proportional to average resolved shear strain $\bar{\gamma}_p$ according to the relation $\varepsilon_p = \mu_e \bar{\gamma}_p$. When $\mu_e$ fluctuates from specimen to specimen due to low number of grains present in the gauge length then the same value of axial stress or strain results in different value of $\bar{\tau}$ or $\bar{\gamma}_p$ which contributes to the scatter observed in fatigue life curves of Inconel 792-5A.

## Conclusions

The following conclusions can be drawn from the detailed study of low cycle fatigue behavior of polycrystals Inconel 792-5A at room temperature and at 900 °C:

1. High-amplitude straining is characterized by initial slight hardening followed by saturation at room temperature and sustained weak softening at high temperature. Low-amplitude cycling results in the stable stress response.
2. The Basquin curve and the cyclic stress–strain curve depend strongly on temperature. Weak temperature effect is apparent on the Manson–Coffin curve in the high-amplitude domain.
3. Cyclic plastic strain localization into PSBs lying parallel to {111} planes was observed at both temperatures.
4. Surface morphology of PSMs depends on temperature. PSMs are straight at room temperature and wavy at 900 °C. Extrusions within PSMs are several times higher at 900 °C than those at room temperature.
5. Temperature dependence of the extrusion height supports vacancy models of surface relief formation.

**Acknowledgements** This research was supported by the Grants Nos. 106/07/1507 of the Grant Agency of the Czech Republic and 1QS200410502 of the Academy of Sciences of the Czech Republic and by the project No. FI-IM/025 of the Ministry of Industry and Trade.

## References

1. Bradley EF (ed) (1988) Superalloys: a technical guide. ASM International, Metal Park
2. Donachie MJ, Donachie SJ (2002) Superalloys: a technical guide. ASM International, Materials Park
3. Beck T, Pitz G, Lang K-H et al (1997) Mater Sci Eng A 234–236:719
4. Shahinian P, Sadananda K (1989) Mater Sci Eng A 108:131
5. Polák J (1991) Cyclic plasticity and low cycle fatigue life of metals. Elsevier, Amsterdam
6. Mughrabi H (1999) In: Wu XR, Wang ZG (eds) Proceedings of the seventh international fatigue congress (FATIGUE '99). Higher Education Press, Beijing, p 1967
7. Merrick HF (1974) Metall Trans 5:891
8. Clavel M, Pineau A (1982) Mater Sci Eng 55:157
9. Fritzemeier LG, Tien JK (1988) Acta Metall 36:275
10. Worthem DW, Robertson IM, Leckie FA et al (1990) Metall Trans A 21:3215
11. Sundararaman M, Chen W, Singh V et al (1990) Acta Metall Mater 38:1813
12. Jiao F, Zhu J, Wahi RP et al (1992) In: Rie K-T (ed) Low cycle fatigue and elasto-plastic behaviour of materials, vol 3. Elsevier, London, p 298
13. Raman SGS, Padmanabhan KA (1994) Int J Fatigue 16:209
14. Betge D, Österle W, Ziebs J (1995) Scr Metall Mater 32:1601
15. Ye D, Ping D, Wang Z et al (2004) Mater Sci Eng A 373:54
16. Petrenec M, Obrtlík K, Polák J (2005) Mater Sci Eng A 400–401:485
17. Obrtlík K, Man J, Petrenec M et al (2002) In: Blom AF (ed) Proceedings of the eight international fatigue congress (FATIGUE 2002). EMAS, West Midlands, UK, p 963
18. Risbet M, Feaugas X, Guillemer-Neel C et al (2003) Scr Mater 49:533
19. Harvey SE, Marsh PG, Gerberich WW (1994) Acta Metall Mater 42:3493
20. Vinogradov A (2007) J Mater Sci 42:1797. doi:10.1007/s10853-006-0973-z
21. Cretegny L, Saxena A (2001) Acta Mater 49:3755
22. Man J, Obrtlík K, Blochwitz C et al (2002) Acta Mater 50:3767
23. Villechaise P, Sabatier L, Girard JC (2002) Mater Sci Eng A 323:377
24. Man J, Obrtlík K, Polák J (2003) Mater Sci Eng A 351:123
25. Polák J, Man J, Obrtlík K (2003) Int J Fatigue 25:1027
26. Polák J, Man J, Obrtlík K et al (2003) Z Metallkd 94:1327
27. Man J, Petrenec M, Obrtlík K et al (2004) Acta Mater 52:5551
28. Cabbibo M, Gariboldi E, Spigarelli S et al (2008) J Mater Sci 43:2912. doi:10.1007/s10853-007-1803-7
29. Blochwitz Ch, Brechbühl J, Tirschler W (1996) Mater Sci Eng A 210:42
30. Mughrabi H, Bayerlein M, Wang R (1991) In: Brandon DG, Chaim R, Rosen A (eds) Proceedings of the ninth international conference on strength of metals and alloys (ICSMA 9), vol 2. Freund, London, p 879
31. Essmann U, Gösele U, Mughrabi H (1981) Philos Mag A 44:405
32. Polák J (1987) Mater Sci Eng 92:71
33. Klesnil M, Lukáš P (1992) Fatigue of metallic materials. Academia, Prague
34. Westbrooke EF, Forero LE, Ebrahimi F (2005) Acta Mater 53:2137
35. Chieragatti R, Remy L (1991) Mater Sci Eng A 141:11
36. Österle W, Betge D, Fedelich B et al (2000) Acta Mater 48:689
37. Lukáš P, Kunz L (2002) Mater Sci Eng A 322:217
38. Polák J (2003) In: Milne I, Ritchie RO, Karihaloo B (eds) Comprehensive structural integrity, vol 4. Elsevier, Amsterdam, p 1
39. Chu Z, Yu J, Sun X et al (2008) Mater Sci Eng A 488:389
40. Krupp U (2008) J Mater Sci 43:3908. doi:10.1007/s10853-007-2363-6
41. Reuchet J, Remy L (1983) Mater Sci Eng 58:19
42. Mughrabi H (1996) In: Lütjering G, Nowack H (eds) Proceedings of the sixth international fatigue congress (FATIGUE '96), vol 1. Elsevier, Oxford, p 57
43. Polák J, Obrtlík K, Hájek M (1994) Fatigue Fract Eng Mater Struct 17:773
44. Obrtlík K, Lukáš P, Polák J (1998) In: Rie K-T, Portella PD (eds) Low cycle fatigue and elasto-plastic behaviour of materials, vol 4. Elsevier, Amsterdam, p 33
45. Mughrabi H (1978) Mater Sci Eng 33:207
46. Kunz L, Lukáš P, Mintách R et al (2006) Metall Mater 44:275
47. Huang Y, Langdon TG (2007) J Mater Sci 42:421. doi:10.1007/s10853-006-0483-z
48. Sauzay M (2007) Acta Mater 55:1193